

GROUND-STATE NUCLEAR PROPERTIES OF NEUTRON-RICH COPPER ISOTOPES AND LEPTON CAPTURE RATES IN STELLAR MATTER

JAMEEL-UN NABI^{a,†}, TUNCAY BAYRAM^{b,‡}, MUHAMMAD MAJID^{a,§}

^aFaculty of Engineering Sciences

GIK Institute of Engineering Sciences and Technology

Topi 23640, Khyber Pakhtunkhwa, Pakistan

^bDepartment of Physics, Faculty of Science, Karadeniz Technical University
Trabzon, Turkey

(Received February 8, 2018; accepted April 10, 2018)

This study essentially consists of two separate investigations where we study neutron-rich isotopes of copper. Two different nuclear models were selected to perform the two investigations. In the first part of this paper, the nuclear ground-state properties of neutron-rich copper isotopes ($72 \leq A \leq 82$) have been studied with the help of the relativistic mean field (RMF) model. The second portion of this paper is dedicated to calculation of lepton capture rates in stellar environment. Ground and excited states of GT and U1F strength functions were calculated in a microscopic way employing the deformed proton–neutron quasiparticle random phase approximation (pn-QRPA) model. The lepton capture rates were computed on a wide temperature range of $(0.01–30) \times 10^9$ K and stellar density range of $(10–10^{11})$ g/cm³. We compared our computed half-lives (GT + U1F) with previous theoretical and measured results. Our calculated terrestrial half-lives agree well with the measured ones. Our study shows that, at high stellar temperatures, allowed GT and, specially, U1F positron capture rates dominate the competing β -decay rates. For a better description of presupernova evolutionary phases of massive stars, simulators are recommended to take into account lepton capture rates on neutron-rich copper isotopes presented in this work.

DOI:10.5506/APhysPolB.49.1531

1. Introduction

It is desirable to use a single nuclear model for prediction of various nuclear ground-state properties over an isotopic chain. Various nuclear models have been employed in the past to do the needful and may broadly be

[†] Corresponding author: jameel@giki.edu.pk

[‡] t.bayram@ktu.edu.tr

[§] majid.phys@gmail.com

classified into three main groups namely: macroscopic models, macroscopic–microscopic models and microscopic models. An example of the macroscopic models would include the Bethe–Weizsäcker mass formula [1]. FRDM (Finite Range Droplet Model) [2] is a good example of macroscopic–microscopic models. The HF (Hartree–Fock) method [3] and the RMF (relativistic mean field) model [4] may be cited as examples belonging to the microscopic genre. Every model has associated pros and cons. Self-consistent calculation using mean field approximation with effective interactions are suitable alternate approaches for a better prediction of nuclear properties of finite nuclei. Recently, the RMF model was employed to calculate ground-state energies, deformations and sizes of 1897 even–even nuclei, for atomic number between 10 and 110, using the nonlinear RMF force NL3* [5]. More recently, a great effort has been done for developing RMF mass model with density-dependent meson coupling interactions comparable to the most accurate non-relativistic microscopic ones [6].

In the first investigation of our study, we employ the axially deformed RMF model with density-dependent functionals to study ground-state nuclear properties of copper (Cu) (neutron-rich) isotopes. Isotopes of Cu are believed to play a key role in the presupernova evolution of massive stars [7, 8]. The RMF model is successful in determining the ground-state nuclear properties close to neutron and proton drip lines. The RMF model, with adjustable small number of parameters, can provide correct predictions of various ground-state properties of isotopes not only along the stability line but also far from it [5, 9–11]. For reliable determination of ground-state properties of copper isotopes, quadrupole moment constrained calculation has been carried out in this model. Potential energy curves (PECs) for $^{71-82}\text{Cu}$, according to the quadrupole deformation parameter (β_2), have been obtained using the RMF model. Lowest binding energy (BE) of PEC for each nuclei was taken as the ground-state BE. The ground-state shape evolution of $^{71-82}\text{Cu}$ nuclei is discussed by using the PEC results. In the present work, calculated values of BE for copper isotopes were compared with the measured values and calculated results of the FRDM model. Proton, neutron and charge radii of a nucleus are important nuclear properties and they are directly related with the size of nuclei. The quadrupole moment of nuclei, which is related to the deformation, is also one of the crucial nuclear properties. In this investigation, we calculate the binding energy, proton and neutron radii, root mean square (r.m.s.) charge radius, deformation parameter and quadrupole moment of neutron-rich copper isotopes ($^{71-82}\text{Cu}$), bearing astrophysical importance, using the RMF model.

Many efforts have been made in recent years to investigate the nuclear masses and charge-changing transition rates of neutron-abundant species at radioactive ion-beam facilities. However, in terrestrial laboratories many of

the exotic nuclear species cannot be studied, and the problem at hand is best resolved by considering theoretical approaches. Studies of the evolution process of massive stars and related nucleosynthesis mechanism have attracted astrophysicists for many decades. An iron core is left behind during the last stage of star burning. Photodisintegration of iron and capturing of free electrons make the core unstable and ensue the collapse. The collapse process is very sensitive to the electron-to-baryon ratio (Y_e) and entropy of the stellar core [12]. The weak-rates, consisting of the lepton capture and emission rates, play a crucial role in controlling these parameters. The simulation of core collapse of massive stars depends heavily on capturing of the electrons [13]. Due to capturing of electrons, the Y_e content is effectively decreased during the initial stages of collapse. Capturing of electrons decreases the number of electrons responsible for degeneracy pressure, while effect of positron capture (PC) acts in the opposite direction. Both processes can lead to generation of (anti)neutrinos which, in turn, lead to streaming out energy and entropy from the stellar core for density range of $\rho \leq 10^{11} \text{ g cm}^{-3}$. The importance of electron capture (EC) during the presupernova evolutionary phases of massive stars may be seen from Ref. [14]. The significance of PC is pivotal in the stellar core, particularly at high core temperatures and low neutron density regions. During such situations, a slightly larger concentration of e^+ particles can be obtained from the stable conditions of $\gamma + \gamma \longleftrightarrow e^- + e^+$ which favors the electron-positron pairs. The chance for the occurrence of equilibrium and the competition between PC on neutrons and EC on protons are considered as the central and decisive constituents for modeling of Type-II supernovae mechanism (for a detailed discussion, see [15]).

In a low temperature range ($\sim 300\text{--}800 \text{ keV}$) and at intermediate stellar densities ($\leq 10^{10} \text{ g cm}^{-3}$), EC generally occurs on nuclei in the vicinity of $A \sim 60$ [16]. As the chemical potential for electrons and the Q -value approach each other, the corresponding stellar weak-rates become much responsive to the detailed analysis of the Gamow-Teller (GT) strength distributions. However, for bigger values of density and temperature, nuclide in the mass range $A > 65$ become more abundant, and the chemical potential for the electrons is appreciably greater than the Q -value. In this scenario, GT centroid energy and total GT strength are pre-requisites for the determination of EC rates. At higher stellar density ($> 10^{10} \text{ g cm}^{-3}$), the electron chemical potential becomes greater than 2 MeV. Under prevailing conditions, forbidden transitions along with allowed GT transitions need to be taken into account for a better description of the presupernova structure. Detailed discussion can be seen in Refs. [16] and [17].

The first-forbidden (FF) transitions may contribute in lowering the half-lives for neutron-rich isotopes. In this regard, a first attempt was made by Homma *et al.* [18] to quantify the contribution of FF transitions to β -decay half-lives ($T_{1/2}$) by employing the proton-neutron quasiparticle random phase approximation (pn-QRPA) model. The QRPA+gross theory framework [19] also considered the effects of FF transitions. More recently, self-consistent density-functional+continuum QRPA Ref. [20] approach, extended by Borzov, reported the allowed and FF half-lives for the r -process simulations. The Borzov study suggests that FF transitions introduce a small appreciable correction to the $N = 50$ and 82 isotones, but significantly reduce the $T_{1/2}$ values near the $N = 126$ isotones. The same FF contribution to total β -decay half-lives was also studied by [21] using the large scale shell model approach. Recently, the deformed pn-QRPA model was used for the calculation of both GT and U1F (having $|\Delta J| = 2$) transitions of $^{72-82}\text{Cu}$ nuclide in stellar scenario [22]. There the authors concluded that, for $^{80-82}\text{Cu}$, a substantial part of the total β^- -decay rates came from U1F strength, in line with the conclusion of Borzov [23]. The strength of U1F to total β^- -decay rates decreases, when stellar density increases. However, the lepton capture rates contribution (both allowed GT and U1F) were not calculated in [22]. The PC rates may compete with the electron emission rates under stellar conditions. Further, the relative contribution of capture rates to the total stellar weak rates was also missing in [22]. In the later portion of this study, we compute EC and PC rates for neutron-rich copper isotopes ($71 \leq A \leq 82$) employing the deformed pn-QRPA model in stellar environment.

In the next section, we discuss the necessary formalism for computation of ground-state properties of Cu isotopes using the RMF model. Here, we also briefly explain the necessary pn-QRPA formalism for the determination of GT strength functions and lepton capture rates (both allowed GT and U1F). Section 3 is devoted to presentation of our calculated results and associated discussions. Finally, Section 4 summarizes our findings.

2. Theoretical formalism

2.1. The RMF model

In the RMF model, a nucleus consists of nucleons and these nucleons interact with each other in such a way that various mesons and photons are exchanged between nucleons [4]. Scalar σ meson, vector ω meson and isovector ρ meson are conventionally taken into account in the RMF model. The σ meson is responsible for the attractive part of the interaction of nucleons, while ω meson is related with the repulsive part. The photon and ρ meson play key roles in correct description of electromagnetic interaction

and isospin-dependent effects in nuclei, respectively. Initially, interactions of mesons among themselves were not considered but the simplest version of RMF model did not account for a correct description of incompressibility for nuclear matter. For this reason, Boguta and Bodmer [24] proposed to include a non-linear self interaction of the σ mesons in the RMF model. This version of RMF model is commonly known as the non-linear RMF model and has been used for the last thirty years for prediction of various nuclear properties of finite nuclei. Different types of RMF models may be found in literature. In these models, non-linear self interaction of the ω and ρ mesons [25, 26] as well as density-dependent meson–nucleon couplings [27–29] are considered. In the present study, an effective density-dependent interaction DD-ME2 [29] and a point-coupling interaction DD-PC1 [30] are considered. For details of point coupling interaction, the authors suggest to study Ref. [30]. Here, we only describe the theoretical formalism of basic features of the RMF Lagrangian density (given below in Eq. (1) with medium-dependent vertices)

$$\begin{aligned} \mathcal{L} = & \bar{\psi}(i\gamma \cdot \partial - m)\psi + \frac{1}{2}(\partial\sigma)^2 - \frac{1}{2}m_\sigma^2\sigma^2 - \frac{1}{4}\boldsymbol{\Omega}_{\mu\nu}\boldsymbol{\Omega}^{\mu\nu} \\ & + \frac{1}{2}m_\omega^2\omega^2 - \frac{1}{4}\vec{\mathbf{R}}_{\mu\nu}\vec{\mathbf{R}}^{\mu\nu} + \frac{1}{2}m_\rho^2\vec{\rho}^2 - \frac{1}{4}\mathbf{F}_{\mu\nu}\mathbf{F}^{\mu\nu} - g_\sigma\bar{\psi}\sigma\psi \\ & - g_\omega\bar{\psi}\gamma \cdot \omega\psi - g_\sigma\bar{\psi}\gamma \cdot \vec{\rho}\vec{\tau}\psi - A\frac{1 - \tau_3}{2}\psi. \end{aligned} \tag{1}$$

In Eq. (1), the masses of mesons (fields) are represented by m_σ (σ), m_ω (ω) and m_ρ (ρ). g_σ , g_ω and g_ρ are the related meson–nucleon couplings of these mesons. They are assumed to be functions of baryon density in practical applications of the density-dependent hadron field theory. m denotes mass of the nucleon represented by the Dirac spinor (ψ). Bold type symbols indicate space vectors. Isospin vectors are indicated by arrows. The Lagrangian given in Eq. (1) is invariant under parity transformation. The expectation value of the pseudoscalar pion field vanishes in the mean field approximation because only solutions with well-defined parity were considered in the study. To reproduce ground-state properties of nuclei and nuclear matter properties, the unknown meson masses and coupling constants were adjusted using a small number of experimental data of few (finite) nuclei. Field tensors for vector fields ω , ρ and photon in Eq. (1) are given by

$$\begin{aligned} \boldsymbol{\Omega}^{\mu\nu} &= \partial^\mu\omega^\nu - \partial^\nu\omega^\mu, \\ \vec{\mathbf{R}}^{\mu\nu} &= \partial^\mu\vec{\rho}^\nu - \partial^\nu\vec{\rho}^\mu, \\ \mathbf{F}^{\mu\nu} &= \partial^\mu A^\nu - \partial^\nu A^\mu. \end{aligned} \tag{2}$$

By using the Lagrangian density in the classical variational principle, the equations of motion can be obtained for the fields. These are a set of coupled equations including Dirac equation for the nucleons and the Klein–Gordon-like equations for mesons and photons. The resulting equations can be solved for deformed axially symmetric case [31]. The PECs of $^{71-82}\text{Cu}$ isotopes have been obtained from the quadrupole moment constrained calculation. In this calculation, the BE at a fixed deformation was computed by constraining the quadrupole moment $\langle Q_2 \rangle$ to a given value μ_2 in the expectation value of the Hamiltonian given as

$$\langle H' \rangle = \langle H \rangle + C_\mu (\langle Q_2 \rangle - \mu_2)^2. \quad (3)$$

C_μ is the constraint multiplier in this equation. The relation between the deformation parameter β_2 and the expectation value of quadrupole moment $\langle Q_2 \rangle$ was taken as

$$\langle Q_2 \rangle = \left(3/\sqrt{5\pi} \right) Ar^2 \beta_2, \quad (4)$$

where $r = R_0 A^{1/3}$ ($R_0 = 1.2$ fm) and A is the mass number of the nucleon. For pairing correlations, the Bardeen–Cooper–Schrieffer (BCS) method was considered and the constant G approximation was used. As proposed by Karatzikos *et al.* [32], a fixed pairing strength G was kept in our calculation.

2.2. The *pn-QRPA model*

We calculate the super allowed Fermi, allowed GT & U1F transitions and stellar lepton capture rates using the *pn-QRPA* model. The Coulomb interaction with the nucleus distorts the electron wave functions and is characterized by the corresponding Fermi functions in the phase-space integrals. We assume that the stellar temperature is sufficiently high, due to which the electrons are not bound to the nucleus. They are described by the Fermi–Dirac energy distribution function. At high stellar temperatures ($kT > 1$ MeV), positrons are created via electron–positron pair production. We will assume that the positrons follow the same energy distribution as the electrons. We later consider the capturing of these positrons in our calculation (a process that competes with the β -decay rates presented earlier in [22]). We further assume in our calculation that, for the range of stellar density considered in this work, the neutrinos and antineutrinos (produced due to lepton capture reactions) escape freely from the stellar core (neutrino capture is not considered in our calculation).

The deformed *pn-QRPA* Hamiltonian may be written as

$$H^{\text{pn-QRPA}} = H^{\text{Nilsson}} + V^{\text{BCS}} + V_{\text{GT}}^{\text{ph}} + V_{\text{GT}}^{\text{pp}}, \quad (5)$$

where H^{Nilsson} is the single-particle Hamiltonian in a deformed Nilsson basis, V^{BCS} represents the pairing interaction solved using the BCS approach, and the last two terms V_{GT}^{ph} and V_{GT}^{pp} are the particle-hole (ph) and particle-particle (pp) GT forces. The Nilsson approach [33] was used for the calculation of wave functions and single particle energies taking into consideration the nuclear deformation. The BCS approximation was carried out for the protons and neutrons, separately, in the deformed Nilsson basis. In our model, the residual interaction occurs in ph and pp channels. The interactions were given in separable forms and their respective strengths were controlled by corresponding model parameters (χ for ph force and κ for pp force). The model parameters were selected in order to best reproduce the experimental half-lives. Our calculation obeyed the model-independent (ISR) sum rule [34]. The value of χ , taken for both allowed GT and U1F, was $61.20/A$. However for allowed GT, $\kappa = 4.85/A$ [MeV], and for the U1F case, $\kappa = 10.92/A$ [MeV fm⁻²] were considered in our calculation. The selected values of χ and κ exhibited an inverse mass dependence as suggested in Refs. [18, 35–37]. Other variables for the capture rates estimation are the pairing gap (Δ_p, Δ_n), nuclear deformation (β_2), Q -values and the Nilsson potential parameters (NPP). The β_2 values were taken from Ref. [38]. Earlier, the stellar electron emission rates for the selected Cu isotopes were computed [22] using deformation from Ref. [38]. We used deformations from the same reference in order to compare our calculated positron capture with the previous calculated β -decay rates in stellar matter which we discuss later. The NPP were adopted from [39] and the oscillation constant (identical for both protons and neutrons) was determined using the relation $\hbar\omega = 41A^{-1/3}$ [MeV]. Pairing gap value of $\Delta_n = \Delta_p = 12/\sqrt{A}$ [MeV] was employed in our calculation. For the determination of Q -values, we used the mass compilation of Audi and collaborators [40].

The weak lepton capture rates were calculated for the following two charge-changing transitions on ^{71–82}Cu:

- (1) Electron Capture: ${}^A_{29}\text{Cu} + e^- \longrightarrow {}^A_{28}\text{Ni} + \nu_e$.
- (2) Positron Capture: ${}^A_{29}\text{Cu} + e^+ \longrightarrow {}^A_{30}\text{Zn} + \bar{\nu}_e$.

The allowed EC/PC weak-rates from the parent k^{th} level to the daughter l^{th} level of the nuclide are given by

$$\lambda_{\text{EC(PC)}}^{kl} = \left[\frac{\ln 2}{D} \right] \left[f^{kl}(T, \rho, E_f) \right] \left[B(\text{F})^{kl} + \left(g_A/g_V \right)_{\text{eff}}^2 B(\text{GT})^{kl} \right]. \quad (6)$$

We took value of D to be 6143 s [41]. In Eq. (6), B^{kl} s represent sum of reduced transition probabilities of the Fermi $B(\text{F})$ and GT transitions $B(\text{GT})$.

The value of (g_A/g_V) , denoting the ratio of axial and vector coupling constants, was taken as -1.2694 [42]. The detailed formalism for calculation of capture rates for allowed transitions under stellar scenario may be seen from Ref. [43].

The UIF stellar lepton capture rates from the parent k^{th} level to the daughter nuclide l^{th} level are given by

$$\lambda_{\text{EC(PC)}}^{kl} = \frac{m_e^5 c^4}{2\pi^3 \hbar^7} \sum_{\Delta J^\pi} g^2 f^{kl}(\Delta J^\pi) B^{kl}(\Delta J^\pi), \quad (7)$$

where $f^{kl}(\Delta J^\pi)$ and $B^{kl}(\Delta J^\pi)$ are the Fermi function and the reduced transition probability for the capture processes. For necessary formalism of calculation of UIF transitions in the deformed pn-QRPA model with separable interaction, see Refs. [22, 36, 37].

The large temperature inside the core of massive stars implies that there is a finite chance of occupations of parent excited levels in stellar matter. The total EC (λ_{EC}) and positron capture (λ_{PC}) rates per unit time per nucleus are finally given by

$$\lambda_{\text{EC(PC)}} = \sum_{kl} P_k \lambda_{\text{EC(PC)}}^{kl}, \quad (8)$$

where P_k represents the probability of occupation of the parent excited level and is determined using the normal Boltzmann distribution. The sum incorporated in Eq. (8) is taken on all the initial and final levels for calculation of total capture rates. Convergence in our capture rate calculations was ensured (we used a large model space of up to the $7\hbar\omega$ in our pn-QRPA calculation).

3. Results and comparison

As mentioned earlier, we employed the RMF model, with density-dependent DD-ME2 and DD-PC1 interactions, to calculate the ground-state nuclear properties of $^{71-82}\text{Cu}$ nuclide. The calculated nuclear properties include binding energy per nucleon (BE/A), radii of neutron and proton, root-mean-square charge radius, electric quadrupole moment and quadrupole deformation parameter (β_2). We also present the ground-state shape evolution of $^{71-82}\text{Cu}$ isotopes based on their PECs.

The calculated PECs from our quadrupole moment constrained RMF calculation, using DD-ME2 and DD-PC1 functionals for $^{71-82}\text{Cu}$, are displayed in Figs. 1 and 2, respectively. The ground state binding energy of each isotope is taken as reference in these figures. ^{79}Cu has shell closure with magic neutron number $N = 50$ and one can expect that it has the spherical shape. This is clearly visible in the PECs of ^{79}Cu both for DD-ME2 and DD-PC1

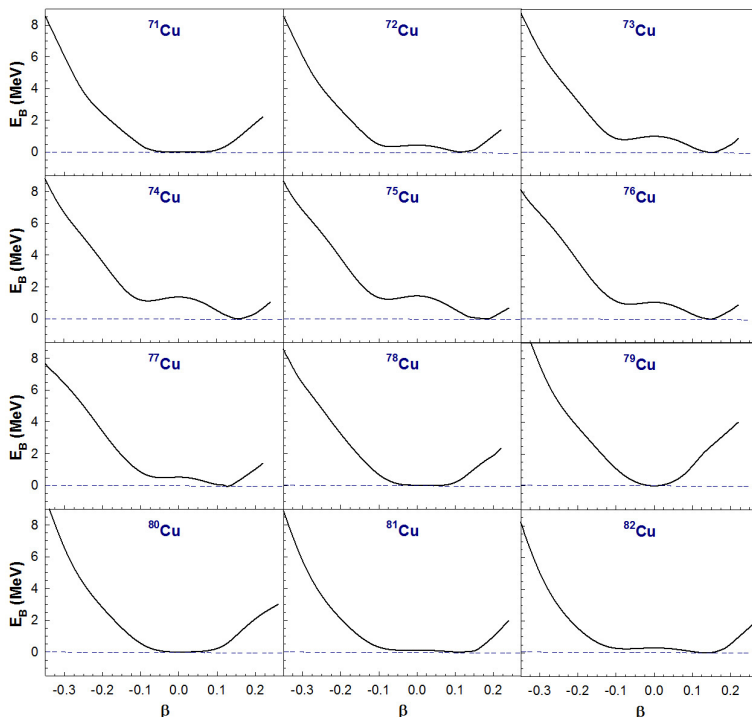


Fig. 1. The potential energy curves for $^{71-82}\text{Cu}$ obtained using the quadrupole moment constrained RMF model with the DD-ME2 interaction.

functionals. It should be noted that neighboring isotopes of closed shell and semi-closed shell nuclei may exhibit spherical character in the RMF model. The neutron number $N = 40$ is known as a semi-magic number. ^{71}Cu has neutron number $N = 42$ which is close to the semi-magic neutron number $N = 40$. For this reason, the ground-state shape of ^{71}Cu is seen as only slightly deformed in both Fig. 1 and Fig. 2. The shape of isotopes starting from ^{72}Cu to ^{77}Cu is seen as prolate in these figures. ^{78}Cu and ^{80}Cu close to neutron shell closure have only slightly deformed shapes. Finally, the shapes of ground-state of ^{81}Cu and ^{82}Cu become prolate again. It is noted from Figs. 1 and 2 that similar PECs are obtained in RMF model with DD-ME2 and DD-PC1 interactions. Based on these PECs, we obtained DD-ME2 and DD-PC1 functional predictions for the ground-state BE/A of $^{71-82}\text{Cu}$ nuclei. The results are shown in Fig. 3. Here, we also show the FRDM predictions [2] and experimental data [40] for the sake of comparison. The calculated BE/A for $^{71-82}\text{Cu}$ using the DD-ME2 interaction in RMF model and the predictions of FRDM model are in agreement with the experimental data. The predictions of DD-PC1 for the BE/A of $^{71-82}\text{Cu}$ are slightly different when they are compared with the results of DD-ME2 interaction.

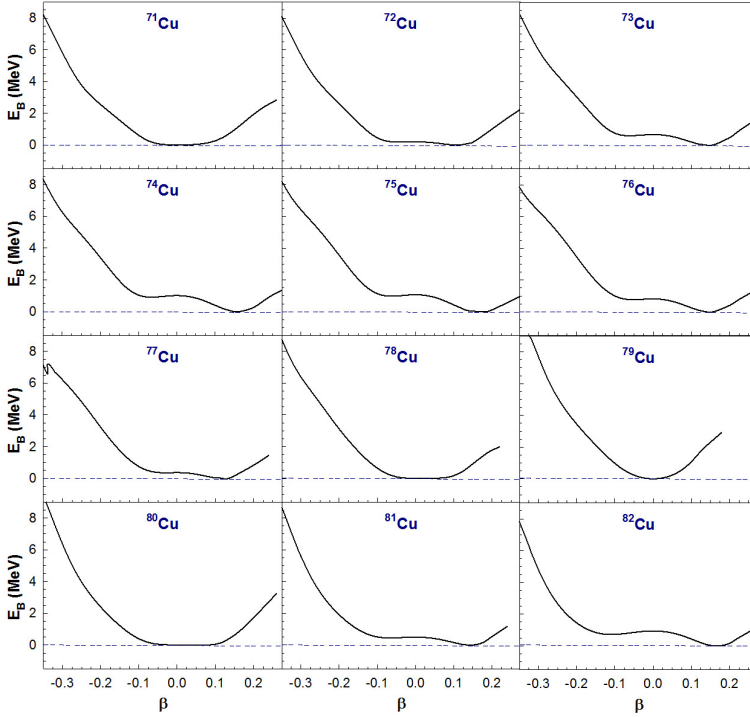


Fig. 2. The potential energy curves for $^{71-82}\text{Cu}$ obtained using the quadrupole moment constrained RMF model with the DD-PC1 interaction.

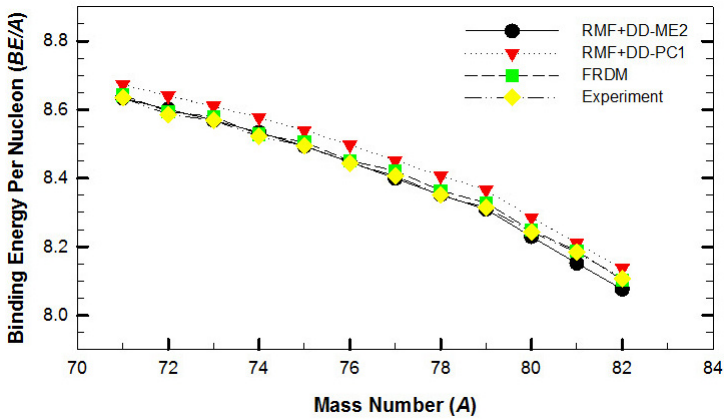


Fig. 3. Binding energy per nucleon for $^{71-82}\text{Cu}$. The predictions of the RMF model, using DD-ME2 and DD-PC1 interactions, are compared with the FRDM calculation [2] and experimental [40] results.

However, the maximal deviation between experimental data and the calculated BE/A using the DD-PC1 interaction is about 0.056 MeV. It should be noted that FRDM gives good results for ground-state binding energies of nuclei throughout the nuclidic chart by fitting many parameters. On the other hand, the RMF model, with smaller number of parameters, shows result at par with the FRDM model [5]. The root-mean-square (r.m.s.) deviation between the calculated values of BE/A using FRDM, RMF+DD-ME2 and RMF+DD-PC1 models and the experimental BE/A values are 0.726, 1.195 and 3.490, respectively. It is concluded that RMF model with DD-ME2 interaction is closer to the FRDM results for predictions of the ground-state BE/A of $^{71-82}\text{Cu}$ isotopes.

Nuclear deformation is one of the important nuclear properties. The RMF model can reproduce the deformations of finite nuclei rather well [44, 45]. In Fig. 4, the calculated quadrupole deformation parameters (β_2) for $^{71-82}\text{Cu}$ using the DD-ME2 and DD-PC1 interactions are shown in comparison with those calculated using the FRDM. As can be seen from Fig. 4, the calculated values of β_2 using the RMF model with DD-ME2 and DD-PC1 functionals for Cu isotopes are close to zero around neutron number $N = 50$ which implies that RMF model predicts the shape of nuclei as spherical at $N = 50$. A similar situation can be also seen in Fig. 5. In this figure, the calculated values of total (neutron+proton) electric quadrupole moments (Q_T) are shown for $^{71-82}\text{Cu}$ isotopes. The results of DD-ME2 and DD-PC1 functionals are close to zero at and near the neutron number $N = 50$. It is observed that the computed values of electric quadrupole moments obtained from RMF model are higher than those from FRDM.

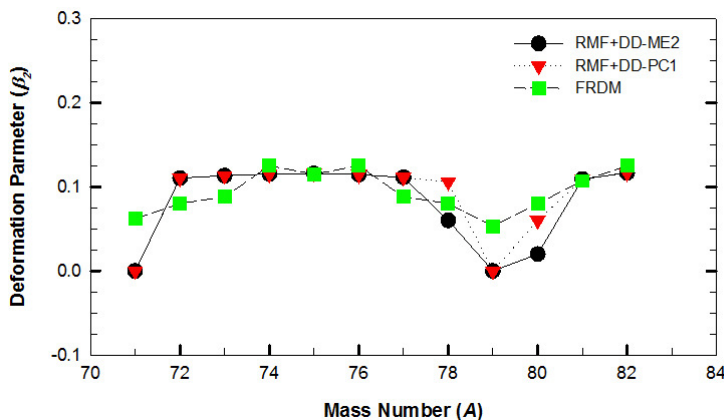


Fig. 4. Calculated quadrupole deformation parameter (β_2) for $^{71-82}\text{Cu}$. The predictions of the RMF model, using DD-ME2 and DD-PC1 interactions, are compared with those of FRDM [2].

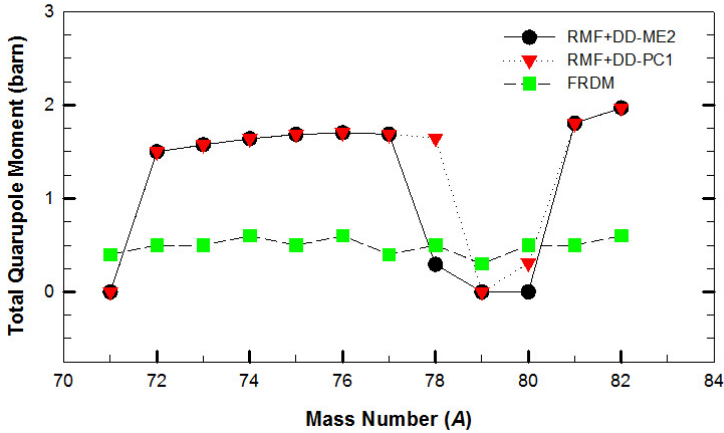


Fig. 5. Total quadrupole moment for $^{71-82}\text{Cu}$. The predictions of the RMF model, using DD-ME2 and DD-PC1 interactions, are compared with the those of FRDM [2].

We calculated neutron and proton radii (r_n and r_p) of $^{71-82}\text{Cu}$ isotopes by considering the DD-ME2 and DD-PC1 interactions. Similar results have been obtained in our calculations for these interactions. Root-mean-square (r.m.s.) charge radius (r_c) of nuclei can be calculated by inserting proton radius (r_p) in the formula $r_c = \sqrt{r_p^2 + 0.64}$ fm. To the best of our knowledge, there is no available experimental charge radii data for $^{71-82}\text{Cu}$. We have listed the calculated r.m.s. charge radii, neutron and proton radii of $^{71-82}\text{Cu}$, using the DD-ME2 interaction, in Table I. The results of our RMF model calculation for BE/A , β_2 and Q_T are also listed in this table.

In the remaining portion of this section, we present discussion on the results obtained from the pn-QRPA model. These results are important for astrophysical applications. We used a quenching factor (f_q) of 0.6 in present pn-QRPA calculation (the same f_q value was suggested for the RPA results in the case of ^{54}Fe nuclide [46]).

To check the reliability of the current pn-QRPA model, we first discuss and compare our calculated terrestrial half-lives ($T_{1/2}$) of copper isotopes with previous measured data and theoretical calculations (Fig. 6). The experimental half-lives were taken from [40, 47] and [48]. Recently, authors of [48] measured the $T_{1/2}$ values for neutron-rich nuclei and it was concluded that the nuclear deformation parameter (β_2) have a sizable contribution to the $T_{1/2}$ values. The authors of [2] used the FRDM+RPA model, by considering only allowed transitions (indicated as Möller *et al.* in Fig. 6). Borzov [49] used the DF3+CQRPA model for the calculation of allowed and U1F charge-changing transitions, by considering spherical nuclide. It was found by Hosmer *et al.* [48] that the spherical shape assumption considered

TABLE I

The RMF calculated ground-state properties of $^{71-82}\text{Cu}$ nuclei using the density-dependent DD-ME2 interaction.

Nuclei	BE/A [MeV]	r_n [fm]	r_p [fm]	r_c [fm]	β_2	Q_T [barn]
^{71}Cu	8.634	4.048	4.853	3.935	0.000	0.000
^{72}Cu	8.601	4.071	4.861	3.943	0.110	1.499
^{73}Cu	8.569	4.107	4.879	3.961	0.113	1.575
^{74}Cu	8.534	4.132	4.890	3.972	0.115	1.640
^{75}Cu	8.494	4.158	4.903	3.984	0.116	1.685
^{76}Cu	8.447	4.166	4.901	3.982	0.115	1.703
^{77}Cu	8.399	4.181	4.906	3.987	0.111	1.688
^{78}Cu	8.351	4.191	4.907	3.988	0.060	0.294
^{79}Cu	8.310	4.204	4.912	3.993	0.000	0.000
^{80}Cu	8.229	4.251	4.921	4.002	0.020	0.000
^{81}Cu	8.152	4.302	4.939	4.019	0.109	1.805
^{82}Cu	8.076	4.345	4.952	4.032	0.117	1.969

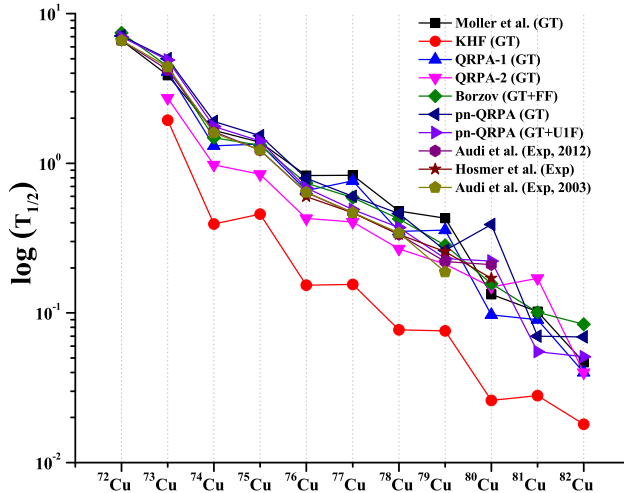


Fig. 6. Calculated terrestrial half-lives ($T_{1/2}$) for copper isotopes using the pn-QRPA model (this work) in comparison with previous theoretical calculations and experimental results. For references, see the text.

in the Borzov work is not justified. KHF, QRPA-1 and QRPA-2 are the results of [50] calculation, in which only allowed GT rates were computed. The deformed pn-QRPA computed half-lives, with and without U1F contribution, are also displayed in Fig. 6. The overall comparison shows that the deformed pn-QRPA model (this work) reproduces well the measured $T_{1/2}$

values as compared to other theoretical models. It is seen that the addition of U1F rates to the allowed GT rates further improves the comparison of our computed half-lives with the measured results. It is noted that the comparison of calculated $T_{1/2}$ values may be improved further by integrating rank 0 and 1 operators (non-unique in nature) in our calculation which we plan to investigate in the near future.

We present the computed allowed GT and U1F strength distributions for neutron-rich Cu nuclei in Fig. 7 and Fig. 8. The allowed GT strengths are shown in arbitrary units, while U1F strength are displayed in fm^2 units. The strength distributions are plotted up to excitation energy of 30 MeV in daughter nuclide. Charge-changing strengths of magnitude less than 10^{-5} , though calculated, are not shown in Fig. 7 and Fig. 8. To further augment the reliability of our calculated lepton capture rates, we integrated the experimental energy levels (XUNDL) in our computation. The pn-QRPA computed excitation energy levels were swapped with the experimental levels when they were within 0.5 MeV of one another. Missing measured energy levels were augmented together with their $\log ft$ values wherever appropriate. Computed levels remain unchanged beyond experimental states for

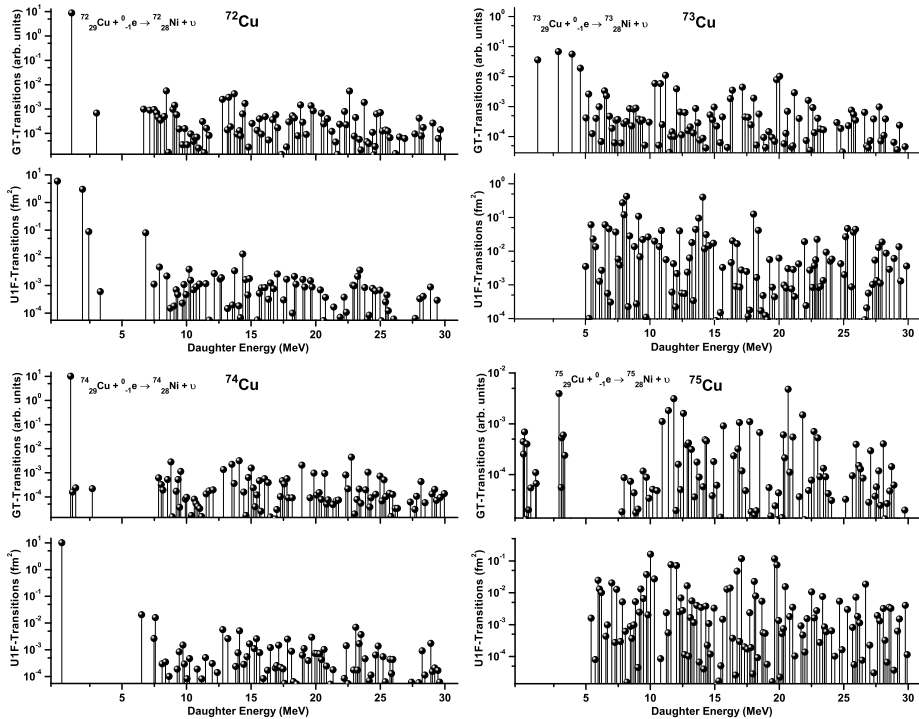


Fig. 7. The pn-QRPA calculated allowed and U1F transitions for $^{72-75}\text{Cu}$ as a function of daughter excitation energy in electron capture direction.

which spin and/or parity assignments were uncertain. Nuclear deformation was taken into account in the current pn-QRPA model which resulted in the fragmentation of GT and U1F transition strengths as shown in the figures. For the heavy copper isotopes, it is noted that U1F transitions appear well above 5 MeV in the daughter excitation energy (Fig. 8). Excited state GT and U1F transitions were also calculated but not presented due to space limitations. The ASCII files of all allowed GT and U1F strength distributions may be requested from the corresponding author.

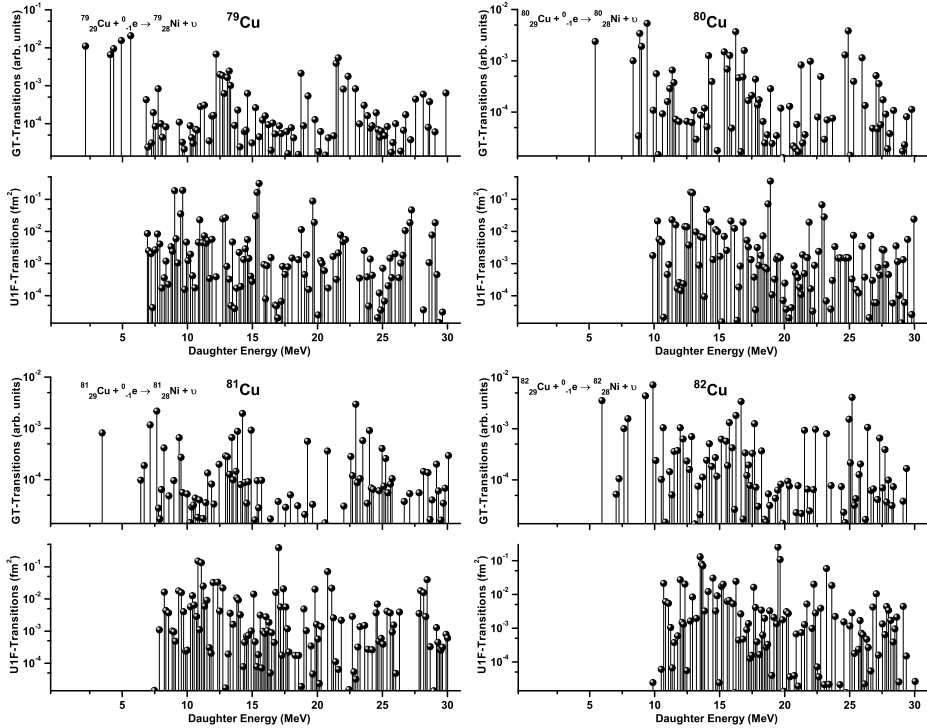


Fig. 8. The same as Fig. 7, but for $^{79-82}\text{Cu}$.

We calculate the EC (λ_{EC}) and PC (λ_{PC}) rates, on copper isotopes, for both allowed GT and U1F transitions, for a broad range of stellar temperature ($0.01 \times 10^9 \leq T(K) \leq 30 \times 10^9$) and density ($10 \leq \rho Y_e \text{ (g cm}^{-3}) \leq 10^{11}$). Figure 9 depicts the calculated EC rates on selected neutron-rich copper isotopes as a function of stellar temperature in units of T_9 (which represent the core temperature in units of 10^9 K). The calculated capture rates are shown at three different stellar density values of 10^3 g cm^{-3} (depicting low-density regions), 10^7 g cm^{-3} (intermediate-density regions) and $10^{10} \text{ g cm}^{-3}$ (high density regions). The pn-QRPA calculated capture rates are given in logarithmic (to base 10) scales. We observe that the calculated EC rates, both

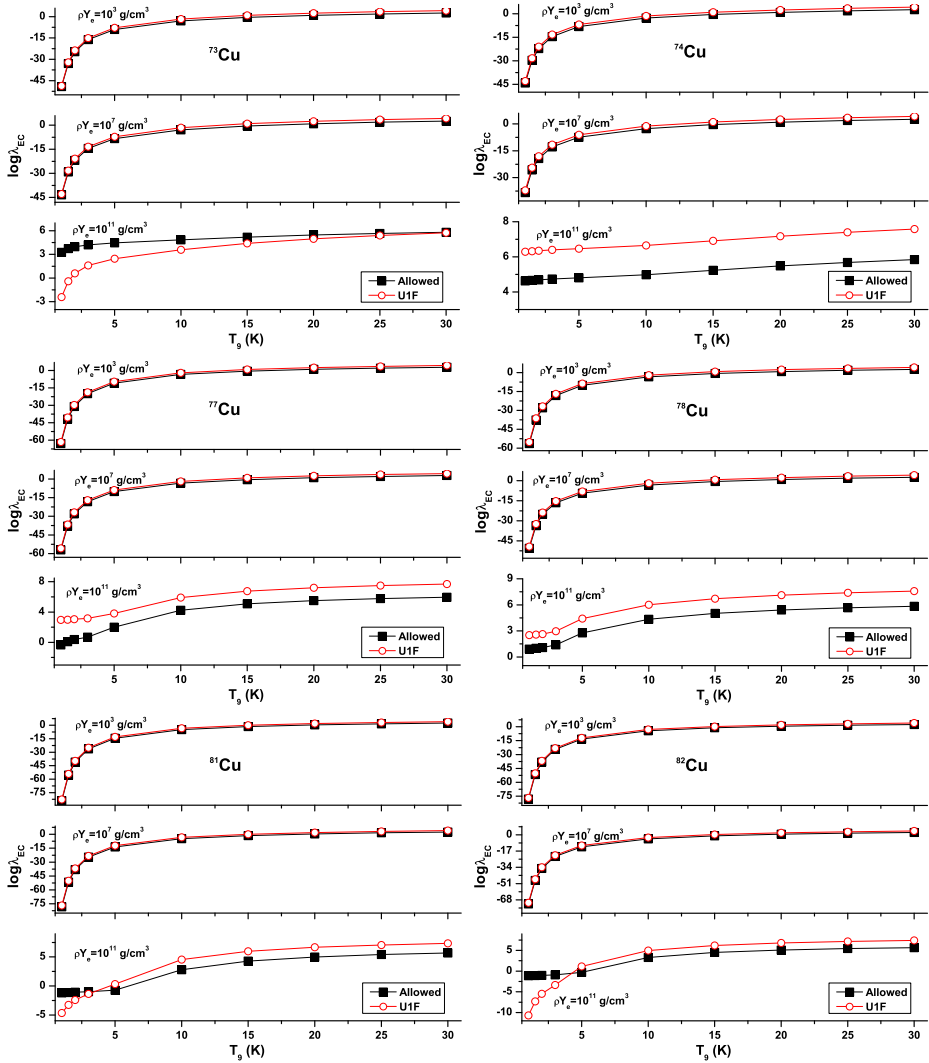


Fig. 9. Calculated allowed GT and U1F electron capture (λ_{EC}) rates on $^{73,74,77,78,81,82}\text{Cu}$ in stellar matter as a function of stellar temperature (T_9) at selected stellar densities. The calculated capture rates are tabulated in log to base 10 scale in units of s^{-1} .

allowed GT and U1F, increase as the stellar temperature and core density rise. Figure 9 clearly shows that the U1F capture weak-rates compete well with the allowed GT capture rates. It is noted that the U1F EC rates are almost greater by an order of magnitude than the allowed GT rates (at low- and intermediate-density regions).

Figure 10 shows similar result for pn-QRPA calculated PC rates on selected copper isotopes. Here, one notes that the allowed GT and U1F rates are almost the same and differ mostly at high stellar temperatures. Tables II, III and IV show the calculated EC and PC rates for $^{72,73,75,76,79,80}\text{Cu}$ isotopes at selected temperature and density values. Once again, all calculated rates are given in log to base 10 scales. Complete ASCII files of lepton capture rates, suitable for interpolation purposes and use in simulation codes, may be requested from the corresponding author.

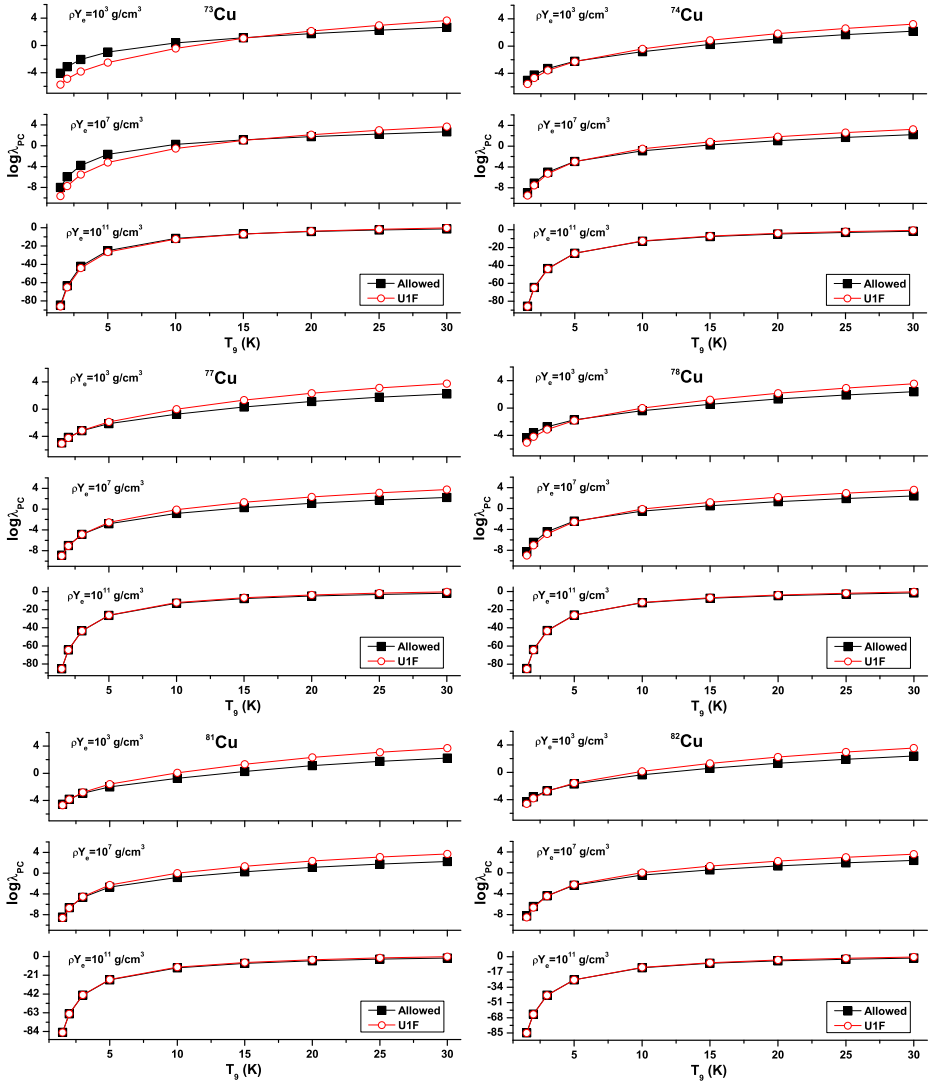


Fig. 10. The same as Fig. 9, but for calculated positron capture rates (λ_{PC}).

TABLE II

Calculated allowed (GT) and unique first-forbidden (U1F) lepton capture rates on $^{72,73}\text{Cu}$ for different selected densities and temperatures in stellar matter. The first column shows the stellar density (ρY_e) (in units of g cm^{-3}). T_9 are given in units of 10^9 K. The calculated capture rates are tabulated in logarithmic (to base 10) scale in units of s^{-1} .

ρY_e	T_9	^{72}Cu				^{73}Cu			
		λ_{PC} (GT)	λ_{EC} (GT)	λ_{PC} (U1F)	λ_{EC} (U1F)	λ_{PC} (GT)	λ_{EC} (GT)	λ_{PC} (U1F)	λ_{EC} (U1F)
10^2	1.5	-5.46	-30.00	-5.47	-28.75	-4.05	-33.03	-5.72	-32.19
	2	-4.68	-22.44	-4.58	-21.19	-3.11	-24.71	-4.88	-23.71
	3	-3.71	-14.69	-3.44	-13.42	-2.05	-16.20	-3.81	-15.06
	5	-2.63	-8.18	-2.08	-6.88	-0.96	-9.10	-2.51	-7.88
	10	-1.15	-2.74	-0.09	-1.37	0.36	-3.04	-0.44	-1.70
	15	-0.09	-0.48	1.27	0.96	1.14	-0.55	1.04	0.91
	20	0.74	0.90	2.28	2.39	1.74	0.89	2.12	2.44
	30	1.39	1.85	3.07	3.40	2.24	1.86	2.96	3.47
10^6	1.5	-7.48	-27.98	-7.49	-26.73	-6.07	-31.00	-7.74	-30.16
	2	-5.96	-21.15	-5.87	-19.89	-4.40	-23.41	-6.17	-22.42
	3	-4.21	-14.18	-3.94	-12.91	-2.55	-15.70	-4.31	-14.56
	5	-2.72	-8.08	-2.17	-6.79	-1.05	-9.01	-2.60	-7.79
	10	-1.16	-2.73	-0.10	-1.36	0.35	-3.03	-0.45	-1.69
	15	-0.09	-0.47	1.26	0.96	1.14	-0.55	1.04	0.91
	20	0.74	0.90	2.28	2.40	1.74	0.89	2.12	2.44
	30	1.39	1.85	3.07	3.40	2.24	1.86	2.96	3.47
10^{10}	1.5	-42.80	1.82	-42.80	3.15	-41.39	0.12	-43.06	-0.42
	2	-32.67	1.87	-32.57	3.20	-31.10	0.42	-32.87	0.59
	3	-22.35	1.96	-22.08	3.30	-20.69	0.83	-22.45	1.60
	5	-13.76	2.12	-13.22	3.47	-12.09	1.35	-13.65	2.45
	10	-6.62	2.52	-5.57	3.91	-5.11	2.23	-5.92	3.58
	15	-3.64	2.98	-2.30	4.43	-2.40	2.90	-2.52	4.38
	20	-1.82	3.41	-0.30	4.92	-0.82	3.40	-0.46	4.96
	30	-0.57	3.77	1.11	5.33	0.29	3.78	0.99	5.40
		0.37	4.06	2.20	5.67	1.14	4.08	2.13	5.75

TABLE III

The same as Table II but for $^{75,76}\text{Cu}$.

ρY_e	T_9	^{75}Cu				^{76}Cu			
		λ_{PC} (GT)	λ_{EC} (GT)	λ_{PC} (U1F)	λ_{EC} (U1F)	λ_{PC} (GT)	λ_{EC} (GT)	λ_{PC} (U1F)	λ_{EC} (U1F)
10^2	1.5	-5.01	-38.87	-5.36	-37.96	-4.24	-34.30	-5.15	-33.06
	2	-4.27	-28.96	-4.53	-27.88	-3.42	-25.54	-4.30	-24.29
	3	-3.39	-18.81	-3.48	-17.58	-2.43	-16.61	-3.22	-15.35
	5	-2.41	-10.33	-2.19	-8.98	-1.35	-9.20	-1.91	-7.91
	10	-1.01	-3.36	-0.20	-1.89	0.04	-3.05	-0.05	-1.68
	15	0.04	-0.68	1.24	0.88	1.01	-0.53	1.22	0.89
	20	0.87	0.82	2.29	2.45	1.77	0.94	2.22	2.42
	30	1.51	1.82	3.08	3.50	2.35	1.92	3.00	3.47
10^6	1.5	-7.03	-36.84	-7.39	-35.93	-6.26	-32.28	-7.18	-31.04
	2	-5.56	-27.67	-5.82	-26.59	-4.71	-24.24	-5.59	-23.00
	3	-3.89	-18.31	-3.98	-17.07	-2.92	-16.10	-3.72	-14.84
	5	-2.50	-10.24	-2.28	-8.89	-1.43	-9.11	-2.00	-7.82
	10	-1.02	-3.35	-0.21	-1.88	0.03	-3.04	-0.06	-1.67
	15	0.03	-0.68	1.24	0.88	1.00	-0.53	1.22	0.90
	20	0.87	0.82	2.29	2.45	1.77	0.94	2.22	2.43
	30	1.51	1.83	3.08	3.50	2.35	1.92	3.00	3.47
10^{10}	1.5	-42.34	-6.89	-42.70	-6.43	-41.57	-2.98	-42.49	-1.66
	2	-32.27	-4.89	-32.52	-3.75	-31.41	-1.58	-32.30	-0.25
	3	-22.03	-2.32	-22.12	-1.01	-21.06	-0.16	-21.86	1.17
	5	-13.54	-0.11	-13.33	1.31	-12.48	1.01	-13.06	2.36
	10	-6.49	1.88	-5.68	3.38	-5.43	2.18	-5.53	3.58
	15	-3.52	2.76	-2.32	4.35	-2.54	2.91	-2.34	4.36
	20	-1.70	3.33	-0.29	4.97	-0.79	3.44	-0.36	4.95
	30	-0.44	3.74	1.12	5.43	0.41	3.84	1.04	5.40
		0.51	4.06	2.19	5.79	1.30	4.15	2.12	5.75

TABLE IV

The same as Table II but for $^{79,80}\text{Cu}$.

ρY_e	T_9	^{79}Cu				^{80}Cu			
		λ_{PC} (GT)	λ_{EC} (GT)	λ_{PC} (U1F)	λ_{EC} (U1F)	λ_{PC} (GT)	λ_{EC} (GT)	λ_{PC} (U1F)	λ_{EC} (U1F)
10^2	1.5	-4.36	-49.99	-4.97	-49.01	-4.37	-45.64	-4.76	-44.41
	2	-3.59	-36.98	-4.12	-35.91	-3.62	-33.81	-3.93	-32.57
	3	-2.67	-23.78	-3.05	-22.61	-2.72	-21.79	-2.88	-20.54
	5	-1.71	-12.90	-1.78	-11.63	-1.75	-11.88	-1.64	-10.60
	10	-0.42	-4.19	-0.04	-2.80	-0.48	-3.89	0.10	-2.53
	15	0.65	-0.98	1.25	0.47	0.44	-0.90	1.27	0.53
	20	1.48	0.75	2.28	2.24	1.19	0.73	2.21	2.22
	25	2.10	1.85	3.07	3.40	1.78	1.79	2.95	3.33
	30	2.58	2.64	3.70	4.23	2.25	2.54	3.56	4.14
10^6	1.5	-6.39	-47.96	-7.00	-46.99	-6.40	-43.61	-6.78	-42.38
	2	-4.87	-35.68	-5.41	-34.62	-4.91	-32.52	-5.22	-31.28
	3	-3.16	-23.27	-3.54	-22.11	-3.22	-21.29	-3.38	-20.04
	5	-1.80	-12.81	-1.87	-11.54	-1.84	-11.79	-1.73	-10.51
	10	-0.43	-4.18	-0.05	-2.79	-0.49	-3.88	0.09	-2.52
	15	0.65	-0.98	1.24	0.47	0.43	-0.90	1.27	0.53
	20	1.48	0.75	2.28	2.24	1.18	0.73	2.21	2.22
	25	2.10	1.85	3.07	3.40	1.77	1.79	2.95	3.33
	30	2.58	2.64	3.70	4.23	2.25	2.54	3.56	4.14
10^{10}	1.5	-41.70	-15.97	-42.31	-17.95	-41.71	-14.79	-42.10	-13.46
	2	-31.58	-12.07	-32.12	-12.12	-31.61	-10.18	-31.92	-8.85
	3	-21.30	-7.39	-21.69	-6.24	-21.35	-5.54	-21.52	-4.21
	5	-12.84	-2.76	-12.92	-1.43	-12.88	-1.77	-12.78	-0.42
	10	-5.88	1.02	-5.52	2.45	-5.94	1.32	-5.39	2.71
	15	-2.89	2.46	-2.32	3.93	-3.11	2.54	-2.29	3.99
	20	-1.07	3.25	-0.30	4.76	-1.37	3.23	-0.37	4.74
	25	0.16	3.77	1.11	5.33	-0.17	3.70	0.99	5.26
	30	1.06	4.14	2.16	5.74	0.73	4.04	2.02	5.65

The ratio of electron to baryon (Y_e) increases as the electron emission (EE) (presented in Ref. [22]) and PC rates increase. One important investigation would be to find out how the two rates compete with each other for these neutron-rich copper isotopes. In Fig. 11 and Fig. 12, the percentage contribution of EE and PC rates are shown. In Fig. 11, the allowed PC and EE rates are shown at $T_9 = 5$ (upper panels) and $T_9 = 30$ (lower panels). The left panels show the situation at low-to-medium density, while the right panels depict the percentage contribution at high stellar density of $10^{11} \text{ g cm}^{-3}$. It is evident from Fig. 11 that PC rates must be taken into consideration at high stellar temperatures as they dominate the competing EE rates for most of the copper isotopes. Figure 12 shows similar results for the UIF rates. At $T_9 = 30$, the calculated PC rates contribute almost 100% for all copper isotopes. For $^{72,73}\text{Cu}$, even at $T_9 = 5$ and low-to-medium density regions, the PC contributes more than 50% to the total weak rates. These findings are crucial and emphasize that *both* EC and PC rates of copper isotopes need to be taken into account in all presupernova evolution simulation codes at high temperatures.

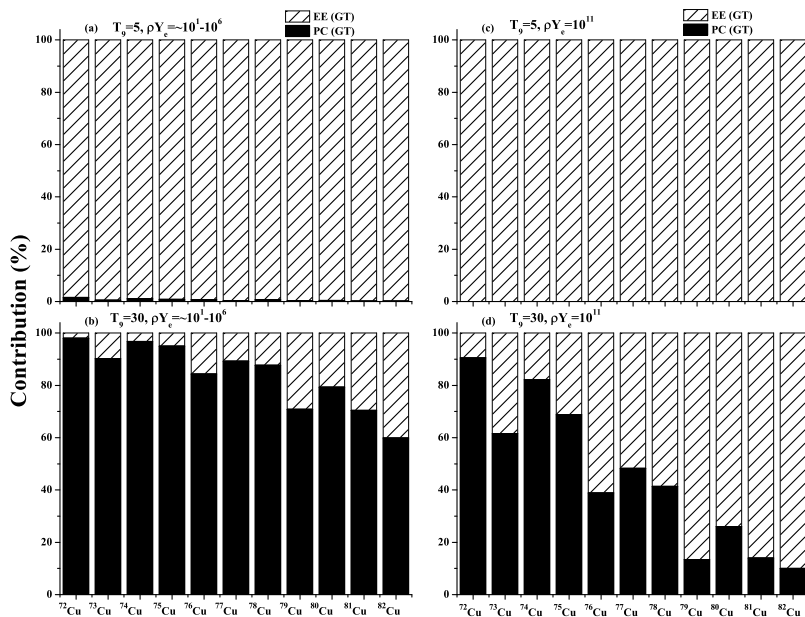


Fig. 11. Percentage contribution of allowed positron capture and β -decay rates for neutron-rich copper isotopes. T_9 are given in units of 10^9 K. Stellar density, ρY_e , is given in units of g/cm^3 .

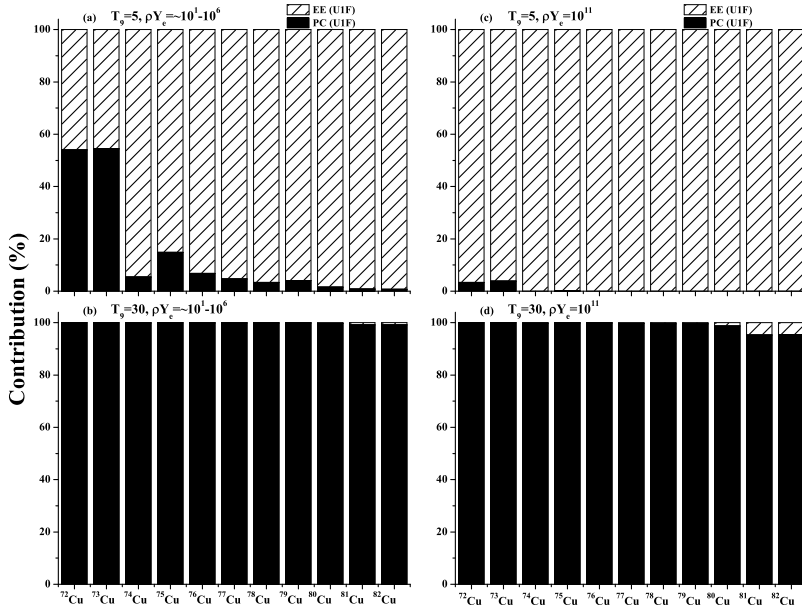


Fig. 12. The same as Fig. 11, but for U1F rates.

4. Conclusions

We used the density-dependent RMF model to study the nuclear ground-state properties of neutron-rich copper isotopes. Two different interactions, namely the DD-ME2 and DD-PC1 interactions, were employed to calculate the binding energy, proton and neutron radii, root mean square (r.m.s.) charge radius, deformation parameter and quadrupole moment of neutron-rich copper isotopes ($^{71-82}\text{Cu}$). The predictions of RMF model with the DD-ME2 functional for BE per nucleon of the isotopic chain were found in agreement with experimental data and the results of FRDM. We obtained PECs of $^{71-82}\text{Cu}$ isotopes using the quadrupole moment constrained RMF model calculation. These PECs indicate that ^{71}Cu and ^{79}Cu nuclei have the spherical shape in their ground-state, while the shape of ^{78}Cu and ^{80}Cu nuclei are close to spherical character. The shapes of others are predicted as prolate in our RMF calculation.

The deformed pn-QRPA theoretical model was used in the second half of this work to calculate lepton capture weak-rates on the copper nuclide in stellar scenario. Here, we used the pn-QRPA model to compute the allowed GT and U1F transition strengths for these copper isotopes. All ground-state and excited states charge-changing strength distributions were computed in a microscopic way. We also calculated the stellar EC and PC rates including both allowed GT and U1F contributions. This completes our initial study,

where we presented the β -decay rates of neutron-rich copper nuclide in stellar matter. The EC rates on copper isotopes were found to be important especially in high-temperature and high-density regions. It was concluded that at high stellar temperature, the PC rates dominate the corresponding β -decay rates and should be taken into account by core-collapse simulators to depict a realistic picture of the process.

J.-U. Nabi would like to acknowledge the support of the Higher Education Commission Pakistan through project number 5557/KPK/NRPU/R&D/HEC/2016 and the Pakistan Science Foundation through project number PSF-TUBITAK/KP-GIKI (02). This research has been supported by the Council of Higher Education of Turkey (Mevlana Exchange Program Based on Project) project number: MEV-2016-094, 2016.

REFERENCES

- [1] C.F.V. Weizsäcker, *Z. Phys.* **96**, 431 (1935).
- [2] P. Möller, J.R. Nix, K.L. Kratz, *At. Data Nucl. Data Tables* **66**, 131 (1997).
- [3] H. Flocard, P. Quentin, D. Vautherin, *Phys. Lett. B* **46**, 304 (1973).
- [4] J.D. Walecka, *Ann. Phys.* **83**, 491 (1974).
- [5] T. Bayram, A.H. Yilmaz, *Mod. Phys. Lett. A* **28**, 1350068 (2013).
- [6] D. Peña-Arteaga, S. Goriely, N. Chamel, *Eur. Phys. J. A* **52**, 320 (2016).
- [7] M.B. Aufderheide, I. Fushiki, S.E. Woosley, D.H. Hartmann, *Astrophys. J. Suppl. Ser.* **91**, 389 (1994).
- [8] A. Heger, S.E. Woosley, G. Martínez-Pinedo, K. Langanke, *Astrophys. J.* **560**, 307 (2001).
- [9] Y.K. Gambhir, P. Ring, A. Thimet, *Ann. Phys.* **198**, 132 (1990).
- [10] P. Ring, *Prog. Nucl. Part. Phys.* **37**, 193 (1996).
- [11] D. Vretenar, A.V. Afanasjev, G.A. Lalazissis, P. Ring, *Phys. Rep.* **409**, 101 (2005).
- [12] H.A. Bethe, G.E. Brown, J. Applegate, *Nucl. Phys. A* **324**, 487 (1979).
- [13] W.R. Hix *et al.*, *Phys. Rev. Lett.* **91**, 201102 (2003).
- [14] H.A. Bethe, *Rev. Mod. Phys.* **62**, 801 (1990).
- [15] J.-U. Nabi, M.-U. Rahman, M. Sajjad, *Braz. J. Phys.* **37**, 1283 (2007).
- [16] H.-Th. Janka, K. Langanke, G. Martínez-Pinedo, B. Müller, *Phys. Rev.* **44**, 38 (2007).
- [17] K. Langanke, G. Martínez-Pinedo, *Rev. Mod. Phys.* **75**, 819 (2003).
- [18] H. Homma *et al.*, *Phys. Rev. C* **54**, 2972 (1996).
- [19] P. Möller, B. Pfeiffer, K.-L. Kratz, *Phys. Rev. C* **67**, 055802 (2003).

- [20] I.N. Borzov, *Nucl. Phys. A* **777**, 645 (2006).
- [21] Q. Zhi, *et al.*, *Phys. Rev. C* **87**, 025803 (2013).
- [22] M. Majid, J.-U. Nabi, G. Daraz, *Astrophys. Space Sci.* **362**, 108 (2017).
- [23] I.N. Borzov, *Phys. Rev. C* **71**, 065801 (2005).
- [24] J. Boguta, A.R. Bodmer, *Nucl. Phys. A* **292**, 413 (1977).
- [25] Y. Sugahara, H. Toki, *Nucl. Phys. A* **579**, 557 (1994).
- [26] J. Piekarewicz, *Phys. Rev. C* **66**, 034305 (2002).
- [27] H. Lenske, C. Fuchs, *Phys. Lett. B* **345**, 355 (1995).
- [28] H. Shen, Y. Sugahara, H. Toki, *Phys. Rev. C* **55**, 1211 (1997).
- [29] G.A. Lalazissis, T. Nikšić, D. Vretenar, P. Ring, *Phys. Rev. C* **71**, 024312 (2005).
- [30] T. Nikšić, D. Vretenar, P. Ring, *Phys. Rev. C* **78**, 034318 (2008).
- [31] T. Nikšić, N. Paar, D. Vretenar, P. Ring, *Comput. Phys. Commun.* **185**, 1808 (2014).
- [32] S. Karatzikos, A.V. Afanasjev, G.A. Lalazissis, P. Ring, *Phys. Lett. B* **689**, 72 (2010).
- [33] S.G. Nilsson, *Mat. Fys. Medd. Dan. Vid. Selsk* **29**, 16 (1955).
- [34] K. Ikeda, S. Fujii, J.I. Fujita, *Phys. Lett.* **3**, 271 (1963).
- [35] J.-U. Nabi, N. Çakmak, S. Stoica, I. Zafar, *Phys. Scr.* **90**, 115301 (2015).
- [36] J.-U. Nabi, N. Çakmak, S. Stoica, I. Zafar, *Eur. Phys. J. A* **52**, 5 (2016).
- [37] J.-U. Nabi, N. Çakmak, M. Majid, J. Salam, *Nucl. Phys. A* **957**, 1 (2017).
- [38] P. Möller, J.R. Nix, W.D. Myers, W.J. Swiatecki, *At. Data Nucl. Data Tables* **59**, 185 (1995).
- [39] I. Ragnarsson, R.K. Sheline, *Phys. Ser.* **29**, 385 (1984).
- [40] G. Audi *et al.*, *Chin. Phys. C* **36**, 1157 (2012); M. Wang *et al.*, *Chin. Phys. C* **36**, 1603 (2012).
- [41] J.C. Hardy, I.S. Towner, *Phys. Rev. C* **79**, 055502 (2009).
- [42] K. Nakamura [Particle Data Group], *J. Phys. G* **37**, 075021 (2010).
- [43] J.-U. Nabi, H.V. Klapdor-Kleingrothaus, *At. Data Nucl. Data Tables* **71**, 149 (1999).
- [44] G.A. Lalazissis, M.M. Sharma, P. Ring, *Nucl. Phys. A* **597**, 35 (1996).
- [45] G.A. Lalazissis, S. Raman, P. Ring, *At. Data Nucl. Data Tables* **71**, 1 (1999).
- [46] M.C. Vetterli *et al.*, *Phys. Rev. C* **40**, 559 (1989).
- [47] G. Audi *et al.*, *Nucl. Phys. A* **729**, 3 (2003).
- [48] P. Hosmer *et al.*, *Phys. Rev. C* **82**, 025806 (2010).
- [49] I.N. Borzov, *Phys. Rev. C* **71**, 065801 (2005).
- [50] B. Pfeiffer, K.-L. Kratz, P. Möller, *Prog. Nucl. Energy* **41**, 39 (2002).